Proceedings of ASME Turbo Expo 2024
Turbomachinery Technical Conference and Exposition
GT2024
June 24-28, 2024, London, United Kingdom

GT2024-129162

DYNAMIC PERFORMANCE AND CONTROL ANALYSIS OF A SUPERCRITICAL CO_2 RECUPERATED CYCLE

Swatara Tucker
TPG, University of Genoa
Genoa, Italy

Simone Maccarini
TPG, University of Genoa
Genoa, Italy

Luca Mantelli
TPG, University of Genoa
Genoa, Italy

Alberto Traverso
TPG, University of Genoa
Genoa, Italy

ABSTRACT

Supercritical CO_2 (sCO2) power cycles represent a promising technology for driving the energy transition. In fact, various research projects around the world are currently studying the possible applications of this technology, which is characterized by high efficiency, competitive costs, compact machinery and enhanced flexibility with respect to competing systems, such as steam-based power cycles. Within this context, the EU-funded SOLARSCO2OL project aims to build a MW-scale sCO2 pilot facility coupled with a concentrated solar power (CSP) plant. A transient model of the demonstration plant was previously developed in the TRANSEO simulation tool by the Thermochemical Power Group (TPG) of University of Genoa to study the operational envelope of the cycle.

In the present work, the model is upgraded to take into account all the relevant fluid-dynamic and thermodynamic phenomena affecting the transient behaviour of the plant. In particular, a detailed crossflow sCO2-air cooler model is now included, which is crucial for assessing the compressor inlet temperature behaviour and controllability. The system has to comply with several constraints, such as compressor surge margin, turbomachinery inlet temperatures, and compressor inlet pressure. The desired net power output should also be guaranteed. The dynamic responses of the system to step variations in various input variables were recorded and used to design and tune the main operational controls. The input variables considered include: 1) compressor rotational speed, 2) anti-surge valve fractional opening, 3) mass flow rate of air through the cooler, 4) mass flow rate of the molten salts through the heater, and 5) CO_2 inventory for injection and extraction of working fluid.

The implemented control structure includes proportional-integral-derivative controllers (PIDs), feedforward action, and their combinations. The controllers are tuned using a mix of established methods, such as Cohen-Coon response-based PID tuning and adjustments from feedforward controls. The feedforward controls were designed taking into account the steady-state values from off-design simulations, as well as the interactions between each controller and the other controlled variables. The final control setup is tested on various power ramps to assess the capability of the prototype cycle in load following and disturbance rejection, showing very good performance in set-point tracking.

1. INTRODUCTION

The use of fossil fuels to generate thermal and electrical power has occurred in conjunction with a significant increase of greenhouse gas concentrations in the atmosphere during the past century [1]. In order to limit the potential impact on climate change, over the past few decades, research institutions and industry have focused on the development of more efficient and environment-friendly technologies.

Within this context, great attention has arisen around supercritical carbon dioxide (sCO_2) cycles to replace the traditional thermodynamic power cycles, such as steam cycles. The choice of using CO_2 as the working fluid is motivated largely by its properties near the critical point, which is relatively close to ambient conditions and easy to reach (T = 31.1°C and p = 73.8 bar) [2]. Due to the properties of sCO_2, it is possible to significantly reduce the compression work if the fluid is near critical conditions, and transferring heat at a variable temperature makes internal heat recuperation more effective [2].

The main advantages of this solution include high efficiency, flexible operation, compactness, and a wide range of possible heat source temperatures (between 200°C [3] and 900°C [4]). This last feature makes it possible to find many different application areas for sCO_2 cycles, such as waste heat recovery [5], nuclear plants [6], fossil fueled power plants [7], concentrated solar power (CSP) [8] and geothermal [9]. Among the disadvantages, the efficiency gain is limited compared to competing working fluids, and the minimum pressure is quite high, resulting in elevated mechanical stresses.

Among the most targeted applications, CSP-sCO_2 plants are particularly interesting due to the use of a renewable energy

source, which can be enhanced in dispatchability through integration with thermal energy storages (TES). Various studies have been carried out to analyze the off-design operation of CSP-sCO_2 plants [10], as well as to optimize and assess their techno-economic performance [11,12]. However, these systems have many operational constraints and are characterized by non-negligible transient phenomena occurring during load variations. Therefore, it is necessary to consider the dynamic behavior of a sCO_2 plant to understand its real capabilities and to design a responsive and effective control system.

Despite this fact, the scientific literature on dynamics and control of CSP-sCO_2 plants, and in general on sCO2 power cycles, is limited. Van der Westhuizen et al. simulated the transient behavior of a CSP-sCO_2 plant, with a focus on the thermodynamics of turbomachinery and solar receivers [13]. Lambruschini et al. developed a dynamic model of a 10 MW sCO_2 recompressed Brayton cycle and simulated the response of the plant during a process disturbance [14]. Moisseytev et al. tested the control system of a nuclear reactor integrated with a sCO_2 cycle in a simulated environment [15]. To the authors' knowledge, no comprehensive study on control design and analysis of complete sCO_2 plants for CSP applications has been presented before.

The present work is part of the SOLARSCO2OL EU H2020 research project, which aims to develop the first MW-scale CSP-sCO_2 plant of Europe [16]. Previously, the Thermochemical Power Group (TPG) of the University of Genoa proposed a control strategy to regulate the SOLARSCO2OL plant in off-design operation and presented a steady-state analysis of its part-load performance [17,18]. A first investigation of the dynamics of the plant was carried out by Gini et al. [17], while a preliminary design of its controller was presented by Maccarini et al. [19].

The main goal of this article is to design and test the control system of the SOLARSCO2OL plant, relying on the TRANSEO dynamic simulation tool [20]. First, the model presented by Maccarini et al. [19] is improved by including a detailed simulation model of the air cooling system. Then, step changes of each control variable are simulated to dynamically characterize the sCO_2 plant. A detailed control design methodology is presented, and the step response results are used to tune the control system. Finally, the controllers are tested on various load ramp variations to understand the capabilities of the plant and to determine the maximum acceptable load variation rate.

2. PLANT LAYOUT

Figure 1 shows the simplified plant layout of the SOLARSCO2OL sCO_2 cycle. The cycle was designed to be integrated with the Évora Molten Salt Platform (EMSP) of the University of Evora, in Portugal [21]. In this configuration, parabolic solar collectors transfer the solar thermal power to molten salts. Then, they flow through a heat exchanger (identified as "Heater" in Figure 1) to be used as the heat source of the sCO_2 cycle. The presence of hot and cold TES in the molten salt loop, together with a bypass line, makes it possible to regulate the heat transfer to the CO_2 flow.

This layout is based on a simple recuperated sCO_2 Brayton cycle, as seen in both Figure 1 and Figure 2. The sCO_2 flow is pressurized by a compressor and pre-heated by a recuperator before entering the heaters (points 1, 2, 3, and 4). Then, it expands in the turbine and the residual heat is used to pre-heat the colder flow within the recuperator (points 4, 5, and 6). Its temperature is then further reduced by an air cooler to reach the desired conditions at the compressor inlet (points 7 and 1, completing the loop).

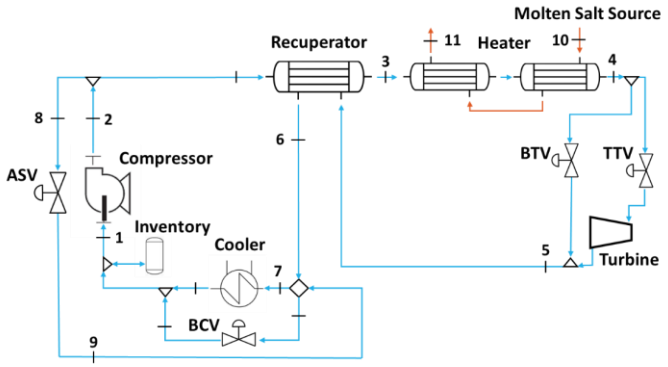

FIGURE 1: PLANT LAYOUT OF THE SOLARSCO2OL SCO_2 CYCLE.

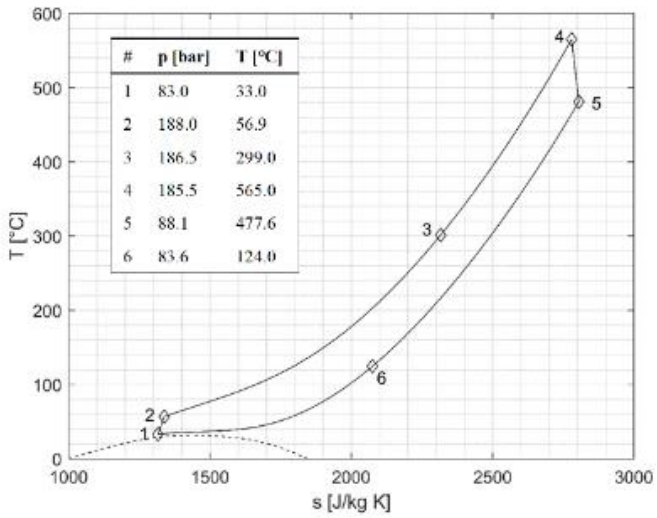

#	p [bar]	T [°C]
1	83.0	33.0
2	188.0	56.9
3	186.5	299.0
4	185.5	565.0
5	88.1	477.6
6	83.6	124.0

FIGURE 2: THE THERMODYNAMIC CYCLE OF SOLARSCO2OL AT ON-DESIGN CONDITIONS.

The system is also equipped with a set of valves to regulate its operation and comply with technical constraints. The compressor inlet pressure is controlled by changing the total CO_2 mass in the loop, which can be added from an inventory or vented; both valves are located at the compressor inlet, and are represented jointly by the "Inventory" in Figure 1. A cooler bypass valve (BCV) can be opened to increase the cooled CO_2 temperature, while an anti-surge valve (ASV) can be opened to

recirculate part of the pressurized CO_2 flow and guarantee safe operation of the compressor. Turbine throttling (TTV) and bypass (BTV) valves are also present; for regular operation, the BTV is closed and the TTV is open.

In order to limit the compression work, the compressor inlet conditions should always be in proximity of the critical point, specifically at 33°C and 83 bar, retaining sufficient margin from the CO_2 bell in order to avoid any condensation at compressor intake. Turbine inlet design conditions are defined as 565°C and 188 bar, respectively. This cycle is designed to have a net efficiency of 21.3%, but an upscaled version of it could achieve values over 31%, as demonstrated by Guedez et al. [22].

3. DYNAMIC MODEL

A dynamic model of the sCO_2 plant was previously developed at TPG to assess the part-load behavior of the system and perform a preliminary analysis of its dynamics [17,18]. The model is based on TRANSEO, a modular tool by TPG that uses the MATLAB-Simulink environment for the dynamic simulation of advanced energy systems based on turbomachinery [20].

3.1. Modelling approach

The compressor and turbine are modelled with a 0D approach. These models determine the relationship between rotational speed, pressure ratio, mass flow, and efficiency of the turbomachinery by interpolating maps. The compressor model also estimates the distance from the surge line by computing the surge margin K_p, defined as the ratio between the current mass flow and the mass flow on the surge line at the same pressure ratio (i.e. mass-flow-based surge margin).

Recuperator and heater models are based on the quasi-2D approach proposed by Traverso et al. [23]. The two fluids, internal solid wall, and external solid wall are all considered separately and discretized along the direction of the flows. The temperatures in each section are updated at each time step by solving the transient energy balance equation over a finite difference numerical scheme, considering the thermal capacity of both solids and fluids.

0D valve models compute the mass flow as a function of the inlet flow temperature and the pressure drop, referring to a reference condition defined by the user.

Recently, Maccarini et al. improved the plant model by implementing an internal estimation of the sCO_2 thermophysical properties, which significantly reduced the simulation time [19]. However, the air cooler was always assumed to be ideal, imposing a CO_2 temperature of 33°C at its outlet. To simulate accurately all the phenomena occurring in the plant, a detailed model of air cooler was developed specifically for this study.

3.2. Air cooler model

The air cooler model is based on the equations and numerical scheme implemented in the code created specifically for CO_2 applications by White et al. [24]. This approach was preferred due to its flexibility and reduced computational time when compared with other air cooler models present in the scientific literature. The code was designed for the sizing of V-shaped dry coolers and developed in Microsoft Excel. Therefore, it was necessary to translate the equations to MATLAB-Simulink and to reorganize them for off-design simulation purposes. The code was also enhanced to simulate both V-shaped and flat dry coolers.

Inside the heat exchanger, the air and CO_2 flow in perpendicular directions, with the CO_2 making multiple passes through the hot tubes. Therefore, the model used a 2D numerical discretization scheme to achieve acceptable accuracy. Figure 3 shows an example of this scheme with 10 subdivisions (N_subs) and 4 passes (n_passes). The model used in this study has 10 subdivisions and 6 passes.

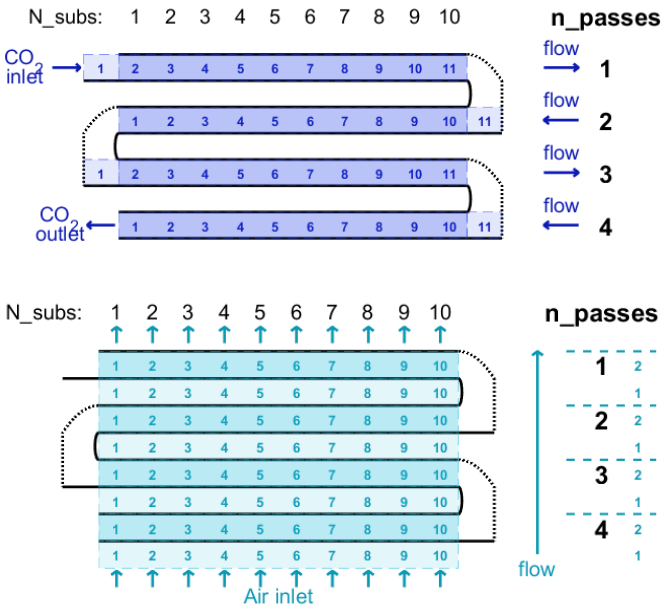

FIGURE 3: EXAMPLE OF NUMERICAL DISCRETIZATION SCHEMES FOR THE CO_2 (TOP) AND AIR (BOTTOM) SIDES OF THE AIR COOLER.

The distributions of air mass flow and inlet temperature are assumed to be uniform, accordingly with other studies regarding the modelling of air coolers [24–26].

The model uses the effectiveness-NTU method to determine the heat exchange between the two flows. The heat transfer coefficient on the air side is computed with different correlations depending on the configuration, specifically those proposed by Wang et al. [27] for V-shaped coolers and those by Kays and London [28] for flat coolers. On the CO_2 side, instead, the heat transfer coefficient is computed with the approach by Cavallini et al. [29] in case of condensation, and with the one by Gnielinsky [30] otherwise.

The simulation relies on multiple iterative loops to determine the performance of the cooler. Starting with the CO_2 inlet at Sub 1 and Pass 1, enthalpy (h) and pressure (p) at each subsection are calculated iteratively based on the subsection preceding it. When the values of p and T of CO_2 and T of the air

and wall at that subsection have converged (error < 0.1%), the next subsection is computed. After the states throughout the entire cooler are calculated, the model checks the error of the air T at each subsection from its previous value (for the first iteration, this is initialized to be the average of the nominal air inlet and outlet temperatures). The model iterates until the sum of these errors along each pass is lower than 0.1%.

Since the discretized cooler model is based on steady-state conservation equations, the transient behaviour has been overlapped through a simplified approach based on time constants; a first order delay is applied to the pressure and temperature of responses on the CO_2 side. The time constants are computed based on the geometrical and thermophysical properties of the heat exchanger and fluids: the calculated CO_2 inlet pressure used a first order time constant of 0.1 seconds, while the time constant associated with temperature was 33 seconds, computed from the heat capacity of the metal (stainless steel) and approximated mass of the metal, as well as the conductive coefficients and area of both flows [20].

The behaviour of the model was then successfully verified against the transient results obtained by Deshmukh et al. [26]. The model was modified based on the actual geometry and calibrated to achieve the same steady state performance, considering the same thermophysical properties of fluids used in [26] for a flat dry cooler. The verification was carried out over 1500 s of simulation, considering multiple step variations of inlet air temperature. Figure 4 shows the agreement of this model with the CO_2 outlet temperature according to the reference model, with an average and maximum error of 0.12°C and 0.33°C, respectively.

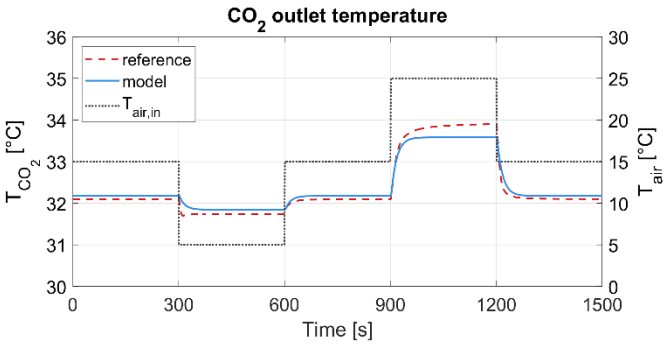

FIGURE 4: VERIFICATION OF THE DYNAMIC AIR COOLER MODEL: CO_2 OUTLET TEMPERATURE UNDER MULTIPLE STEP VARIATIONS OF INLET AIR TEMPERATURE.

Experimental data from the SOLARSCO2OL demonstration plant will become available over time, at which point the model can be verified further.

4. CONTROL DEVELOPMENT AND DESIGN

There are five parameters of the system that were determined to need proper controls: the compressor inlet pressure (CIP), compressor inlet temperature (CIT), and turbine inlet temperature (TIT), to be kept within acceptable ranges; the surge margin (K_p), to be kept above a safety threshold; and the plant net power (P_{net}), which should follow the power demand setpoint. As identified by Gini et al., these conditions could be guaranteed by manipulating, respectively: 1) the total mass of CO_2 in the system, 2) the cooler bypass valve fractional opening or mass flow rate of air through the cooler, 3) the mass flow rate of molten salt through the heater, 4) opening of the anti-surge valve, and 5) the compressor speed [17,18]. However, operating the cooler at maximum power and acting on the bypass valve to control the CIT would only be useful in case of a drastic drop in temperature, as it would cause inefficiencies at all other times. Since the cooler air flow can be directly controlled by changing the fan rotational speed, this option was preferred in this study.

Table 1 shows the manipulated variables and their control structures, alongside the constraints that they are meant to meet. Under the control structure column, "FF" represents a feedforward control, while "PI" and "PID" signify proportional-integral and proportional-integral-derivative controllers respectively. The CIT controller is exclusively feedback, and the net power and surge margin controllers are exclusively feedforward. The CIP and TIT controllers use combinations of feedforward and feedback: the TIT controller due to its long (>300 seconds) settling time in response to a step change (as seen in Figure 7), and the CIP controller due to its complicated nonlinear dynamics (as seen in Figure 5).

TABLE 1: CONTROL TARGETS AND STRUCTURE

Constrained variable	Target value	Max Tolerance	Manipulated variable	Control structure
CIP [MPa]	8.30 MPa	± 0.075 MPa	Addition or removal of working fluid	FF adjusted w/ error + PI
CIT [°C]	33°C	± 1°C	Cooler air flow rate	PI
TIT [°C]	565°C	± 5°C	Molten salt flow rate	FF + PID
K_p [-]	1.11	> 1.1 constraint	Anti-surge valve FO	Predictive FF
P_{net} [%]	50% to 100%	Error <1% of setpoint	Compressor speed	FF

4.1. Compressor inlet pressure controller

The compressor inlet pressure is regulated by injection or extraction of mass from the system at the compressor inlet. The inventory container is not modelled directly, but its internal pressure is imposed as a boundary condition of its valve. The controller dictates the desired mass flow rate of CO_2 to be added or removed from the system, and a valve to the atmosphere or from the inventory is opened to achieve this mass flow rate. The CIP control is composed of a manually-tuned proportional-integral (PI) controller, which is combined with an feedback-adjusted FF controller based on the compressor speed. With low gains, the PID control alone could not effectively regulate the pressure, while higher gains would result in oscillations, causing instabilities such as repeated venting and addition of working

fluid. The base FF controller, before the error adjustment, determines the desired steady-state long-term action of the inventory based on the steady-state map of total CO_2 mass as a function of compressor speed. However, due to the nonlinear dynamic response of the plant, as seen in Figure 5, the controller action would have an excessive short-term impact on the CIP. The difference between long-term and short-term effect can be seen in Figure 5, and depends greatly on the mass flow, represented by the number of seconds taken to add the same mass of CO_2. The inventory mass flow rate also has a large short-term impact on the mass flow through the compressor, given the placement of both the inventory and venting valves near the compressor inlet. This in turn has a large impact on the surge margin, with the fastest addition causing a transient drop greater than 0.1 in the surge margin.

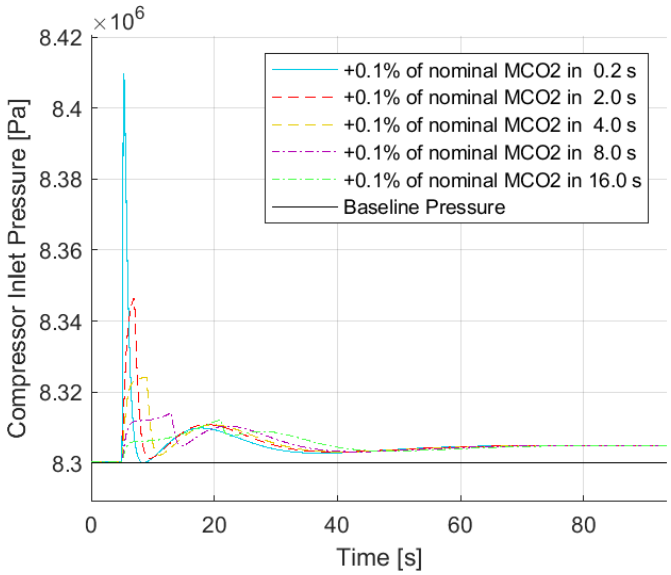

FIGURE 5: VARIOUS RATES OF ADDITION OF 0.1% OF NOMINAL MASS OF CO_2, SHOWING THE DIFFERENCE IN SHORT-TERM VERSUS LONG-TERM RESPONSE.

Figure 6 shows a sketch of the overall control scheme for the compressor inlet pressure. To accommodate the response curves shown in Figure 5, only a fixed percentage of the FF action is guaranteed by the controller, M_{FF} (as represented by the purple line in Figure 6). The remainder of the requested action is then stored in the controller's cumulative memory, M_{FFM}. This memory is equivalent to an integral measure of the error between the actual controller output (represented by the red line) and the requested feedforward output (represented by the dark blue line). This integral is visualized as the sum of the green and orange shaded areas. Then, M_{FB} (an error-dependent fraction of M_{FFM}) is added to M_{FF}, and the final output of the controller is further adjusted by a PI controller, in order to account for transient deviations in the opposite direction to the feedforward action.

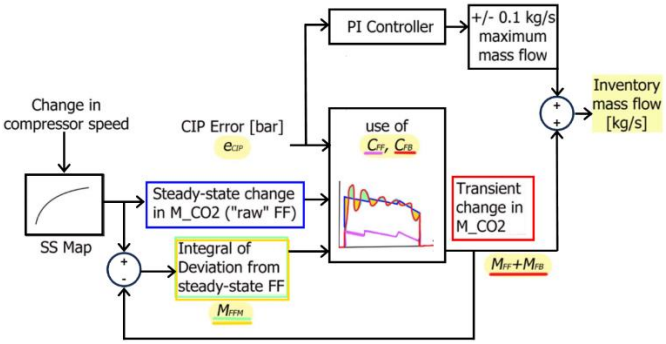

FIGURE 6: EXAMPLE OF ERROR-ADJUSTED FEEDFORWARD INVENTORY CONTROL SCHEME FOR CIP. THE RAW FEEDFORWARD OUTPUT IS SHOWN IN BLUE, WITH THE GUARANTEED OUTPUT IN PURPLE, INTEGRAL OF FEEDFORWARD ERROR ("CUMULATIVE MEMORY") IN GREEN AND ORANGE, AND ACTUAL OUTPUT IN RED.

Specifically, the internal feedback part of the controller, M_{FB}, is proportional to the square of the CIP error, as well as the integral of the error of the actual controller output from the requested controller output (M_{FFM}), up to an imposed limit M_{max}, as shown in equation (1). The coefficient C_{FFM} contains the relation to the error, e_{CIP}, which is defined as shown in equation (2) when the error and memory agree in sign, and is defined as shown in equation (3) otherwise. The feedback coefficient C_{FB} is defined as always positive, such that within equation (2), the value of C_{FFM} is always between $C_{FFM,min}$ (a tunable parameter between 0 and 1, representing the value of C_{FFM} at zero error) and 1 (when $e_{CIP}^2 \cdot C_{FB} \geq 1 - C_{FFM,min}$), while within equation (3), the value of C_{FFM} is always between 0 (when $e_{CIP}^2 \cdot C_{FB} \geq C_{FFM,min}$) and $C_{FFM,min}$ (at zero error).

In this study, C_{FB} was set to 4.0 and $C_{FFM,min}$ was set to 0.01 for best performance. This ensures that, as long as the feedforward memory and error are in the same direction, the mass added by the feedback portion of the inventory control will lie between 1% and 100% of the feedforward memory, up to a maximum mass flow rate. If the error and feedforward memory are in opposing directions, M_{FB} will instead be between 1% and 0%, to retain continuity.

$$M_{FB} = C_{FFM} * M_{FFM} \leq M_{max} \quad \text{and} \quad \geq -M_{max} \tag{1}$$

$$C_{FFM} = C_{FFM,min} + (e_{CIP}^2 * C_{FB}) \leq 1 \tag{2}$$

$$C_{FFM} = C_{FFM,min} - (e_{CIP}^2 * C_{FB}) \geq 0 \tag{3}$$

The feedforward output itself, M_{FF},was set to equal 18.56% of the requested output at each timestep (a number related to the ratio between the short-term and long-term responses shown in Figure 5). The additional PI controller was then tuned manually, starting from values given by the Ziegler-Nichols oscillation tuning method.

4.2. Turbine and compressor inlet temperature controllers

The turbine inlet temperature controller is a combination of a FF and a PID. In this case, the feedforward controller is necessary to compensate for the long (>300 seconds) settling time of the TIT. The FF determines the steady-state value of molten salt mass flow rate through the heater based on a steady-state, off-design map of the mass flow rate of CO_2 at the heater inlet. The FF output is then added to a PID controller output, which compensates for any remaining deviation from the setpoint.

The compressor inlet temperature controller is a PI which regulates the air mass flow rate of the cooler. The monitored variable can be CO_2 temperature or density, as proposed by Casella et al. [31]. Since limitations on sensor noise and signal accuracy were not accounted for in the model, there was no observed difference in performance monitoring the error on density or temperature. For the sake of brevity, the following results only refer to the temperature-based controller.

Both the TIT PID and the CIT PI were tuned following the Cohen-Coon method. The relevant step response curves, as well as the maximum slope tangent used for the tuning, is shown in Figure 7, while the resulting coefficients are presented in Table 2. These coefficients were then empirically adjusted to improve performance. Specifically, they were divided by a factor of 20 for the TIT controller, and multiplied by 3 for the CIT controller.

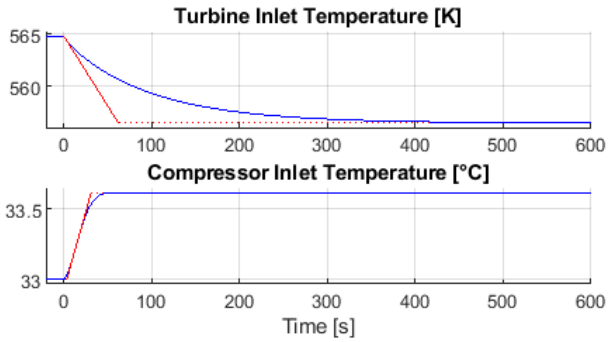

FIGURE 7: STEP RESPONSE CURVES FOR A STEP CHANGE IN MASS FLOW RATE OF MOLTEN SALT (TOP) OR COOLER AIR MASS FLOW (BOTTOM).

TABLE 2: COHEN-COON PID COEFFICIENTS FOR INLET TEMPERATURE CONTROL OF THE COMPRESSOR / TURBINE

Controlled variable; controller type	KP	KI	KD
CIT; P controller	1.3136	-	-
CIT; PI controller	1.1471	0.12178	-
CIT; PID controller	1.7199	0.20516	2.1932
TIT; P controller	3.8422	-	-
TIT; PI controller	3.4554	5.3587	-
TIT; PID controller	5.1206	10.6972	0.36237

In this study, no variations of ambient conditions are considered. Based on some preliminary results, which are not reported here for the sake of brevity, the PI is expected to properly control the CIT (deviation from setpoint within 0.1 to 0.2 °C) in case of moderate (1 to 3 °C per second) variations of the ambient temperature. However, corrective actions (e.g., gain-scheduled PI or integration with FFs) could be implemented in the future to handle more significant deviations.

4.3. Surge margin controller

The anti-surge valve fractional opening (FO_{ASV}) can be increased to recirculate part of the compressor outlet flow to the cooler inlet, moving the operative point away from the surge line. The distance from the surge line is represented by the surge margin (K_p), which is defined as the ratio between the current reduced mass flow and the reduced mass flow on the surge line for the same pressure ratio. A K_p of 1.1 or greater is considered stable operation, and a K_p between 1.0 and 1.1 is considered hazardous operation. A FF controller based on the net power setpoint and compressor speed was used to determine the appropriate FO_{ASV} to maintain K_p above 1.1. At each compressor speed, a steady-state off-design map of K_p by compressor speed is used to predict the value of K_p with FO_{ASV} of 0.00, as shown in Figure 8 with a dashed blue line. Then, the ramp rate of the net power setpoint at that timestep is used to obtain a dynamic offset from the steady-state, as shown in Figure 8 by the red line. The actual K_p computed by the model is shown by the light blue line. Then, this estimated dynamic K_p based on the compressor speed and ramp rate in power is compared to the threshold of 1.11, as listed in Table 1. The FO_{ASV} can then be computed proportionally to the predicted error from this target value to obtain the controller output.

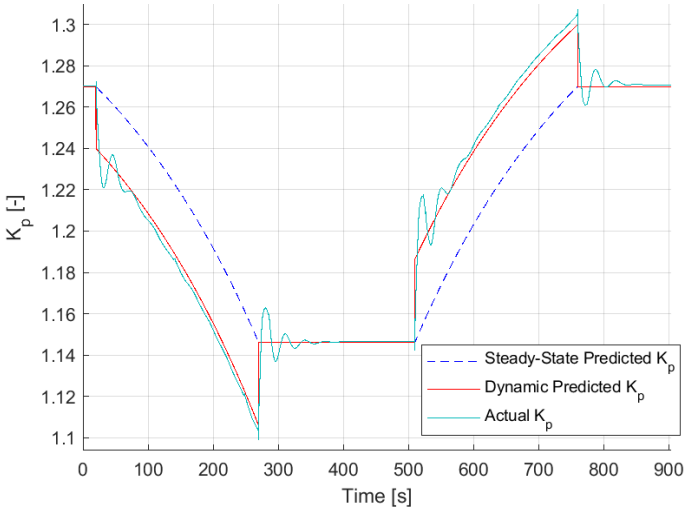

FIGURE 8: PREDICTION OF SURGE MARGIN DURING RAMP IN POWER FOR RAMP RATE OF 12.0% LOAD/MIN.

5. RESULTS AND DISCUSSION

In order to verify the effectiveness of the control logics, various tests have been made, imposing a desired load ramp, and letting the system follow it. The load ramps were set from 100% to 50% of the nominal load and from 50% to 100% of the nominal load, covering the entire range of the system for part-

load operation, according to Gini et al. [18]. Different ramp rates were simulated to understand the limitations of the system and identify the maximum feasible speeds. Ramp rates between 3.0% of nominal load per minute and 15.0% of nominal load per minute were considered.

Figure 9 shows the net power generated by the plant during the ramps from 100% to 50% load and from 50% to 100% load at various ramp rates. The maximum deviation from the setpoint, occurring at the ends of each ramp, was found to be about 2.0 kW per 1.0% load/min of ramp rate. In Figure 9, a maximum deviation was observed for the ramp rate of 15.0% load per minute, of +33.03 kW (+2.2% of nominal load) at the end of the ramp-up, and of -32.21 kW (-2.1% of nominal load) at the end of the ramp-down.

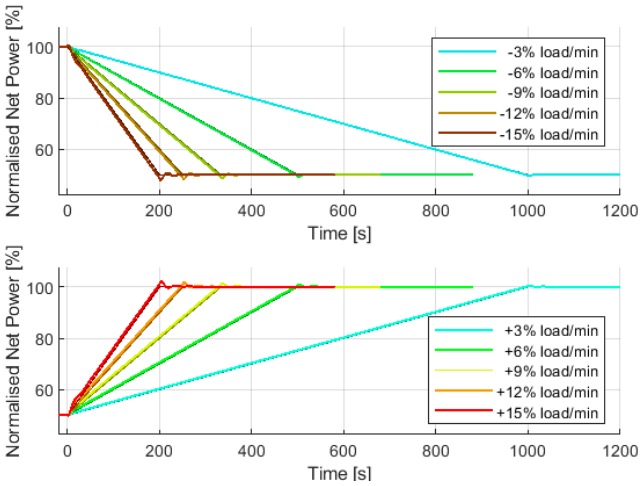

FIGURE 9: MEASURED NET PLANT POWER FOR RAMP DOWN (100% TO 50% LOAD; TOP) AND RAMP UP (50% TO 100% LOAD; BOTTOM).

Figure 10 shows how the same ramps move the compressor operating point on its characteristic map. In the case of ramp-down from the design point (marked by the transition from black "x" to black "o" in the figure, with dashed lines in a mildly darker color), the compressor speed is reduced, decreasing the mass flow rate of the system. The active controls in the system regulate the compressor inlet pressure and temperature, as well as turbine inlet temperature, to stay as near to the design point as possible. Therefore, the decreased mass flow rate through the compressor causes the operative point to move towards the left side of the map at the beginning of each ramp-down in load. From the steady-state condition at 50% load, marked with a black "o" shape, the ramp-up of the system back to design point is represented by the brighter curves on the right side.

Steeper ramps lead to higher variation of the reduced mass flow rate for the same pressure ratio, meaning that the descending and ascending curves on the map show a larger impact on the surge margin (lower mass flow during ramp-down and greater mass flow during ramp-up), which can be observed visually in Figure 10 as a mostly-horizontal deviation from the steady-state off-design path between the two states. The qualitative behaviour during the ramp was similar across all of the ramp rates analysed, with the only notable difference being the magnitude of the offset from the steady-state off-design curve. Descending ramps above 9% of load per minute temporarily lead the system to a condition where $K_p < 1.1$ (within the shaded red region towards the left side of Figure 10). Despite being outside the surge region, this condition is considered hazardous in this study, and would cause a limited opening of the anti-surge valve to compensate. On the other side, when increasing the load, no operational limit is exceeded.

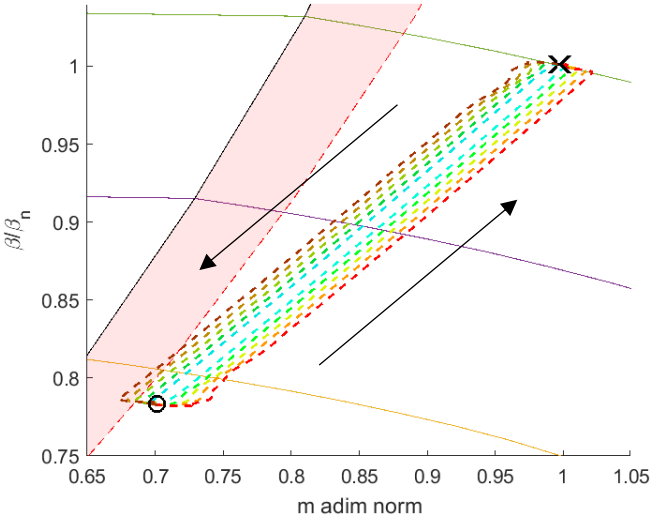

FIGURE 10: COMPRESSOR OPERATING POINTS VISUALIZED ON THE CHARACTERISTIC MAP.

Figure 11 shows the temperatures at the compressor and turbine inlets during the same ramp-down and ramp-up, with ramp rates between 3% load/min and 15% load/min. The CIT remains within 0.02 K of its setpoint, and the TIT remains within 0.17 K of its setpoint. Both the CIT and TIT are therefore considered well-controlled. The x-axis does not represent actual time, but a percentage of "ramp progress" such that the offset caused by the variant ramp rates is clear.

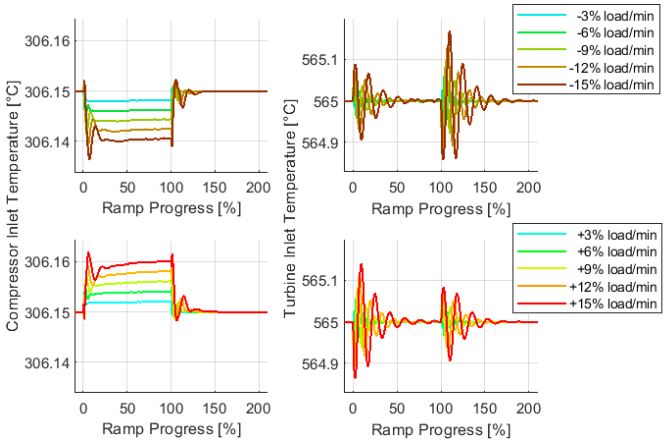

FIGURE 11: VARIATION OF CIT AND TIT DURING A RAMP-DOWN (100% LOAD TO 50% LOAD, TOP) AND RAMP-UP (50% LOAD TO 100% LOAD, BOTTOM), BY RAMP PROGRESS.

As shown in Figure 12, for a change in load between 100% and 50%, irrespective of ramp rate, the same change is required in the total mass of CO_2 enclosed in the system. In particular, to reduce the power to 50% of the nominal load, 106 kg must be removed from the system. This corresponds to a variation of about 9.5% from the nominal point. Likewise, for an increase from 50% load to 100% load, the same quantity of mass should be added to the system from the inventory. According to the specifications of the SOLARSCO2OL pilot plant, addition of mass to the system is achieved using a valve from the inventory, while the removal of mass from the system is achieved with a venting valve. In a non-pilot plant, it would be beneficial to recirculate removed CO_2 into the inventory, to reduce both operational and environmental costs.

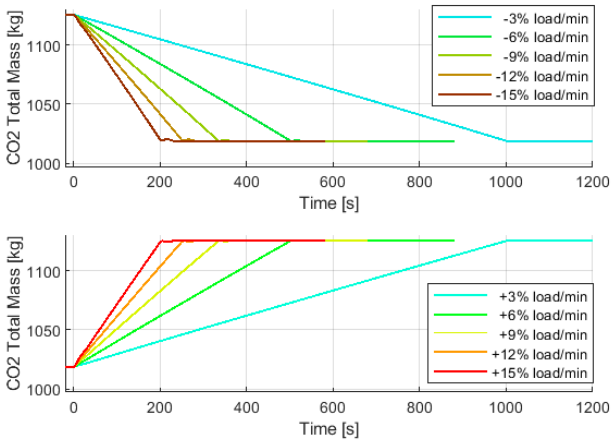

FIGURE 12: TOTAL MASS OF CO_2 INSIDE THE LOOP FOR VARIOUS RAMP RATES IN LOAD.

Figure 13 shows the mass flow of CO_2 removed or added at the compressor inlet to achieve the mass variation shown in Figure 12 to control the compressor inlet pressure. As expected, faster ramps require a larger mass flow rate, as the integral of each of these curves will be equivalent between any two controlled steady-state points. Some overshoot, which can be seen at the start of the ramp in Figure 13, is necessary to mitigate the large increase in pressure associated with compressor deceleration during ramp-down (top), as well as the large decrease in pressure associated with compressor acceleration during ramp-up (bottom). Therefore, despite the apparent oscillations, this control action is considered to be acceptable.

Figure 14 shows the variation of compressor inlet pressure during the same load ramps. It can be seen that even for the steepest ramp, the controllers are able to maintain the pressure within the manufacturer-recommended tolerance (83.00 ± 0.75 bar). It is important to highlight that, even if the control system works properly, variations of pressure are critical and must be properly addressed during the design and testing of the real plant. It can also be observed from Figure 14 that when the compressor speed is increased (end of ramp-down and start of ramp-up), there is a sudden decrease in inlet pressure, and this drop in pressure is more severe for higher ramp rates.

Negative CIP disturbances in particular must be carefully monitored, as they bring the system closer to the critical pressure. In addition, the inventory control system is less effective at increasing the compressor inlet pressure than it is at reducing it, since any mass removal will result in a greater change as a percentage of its final value than the same change in mass in the positive direction. This can be observed in the magnitude of the first peak in Figure 14, where for the same ramp rate, the disturbance in the positive direction (top-left figure, ramp-down) is well-compensated for and only reaches a maximum of around 0.02 MPa, while in the negative direction (bottom-left figure, ramp-up), the disturbance reaches about 0.03 MPa. The same can be observed from the end of the ramp in the same figure, showing that this is not simply a consequence of a disturbance at 50% load as compared to 100% load. This effect was observed in the open-loop changes in the mass of CO_2 as well.

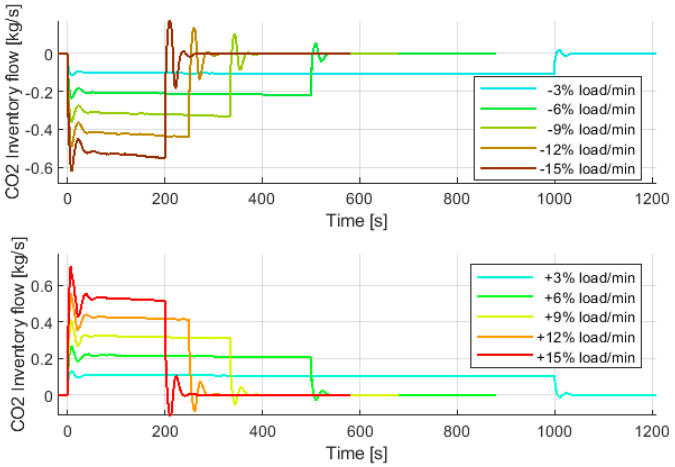

FIGURE 13: INVENTORY CONTROL DURING DIFFERENT RAMP-DOWN ANALYSIS, SCALED DURING THE RAMP TO REFLECT RAMP PROGRESS IN PLACE OF TIME.

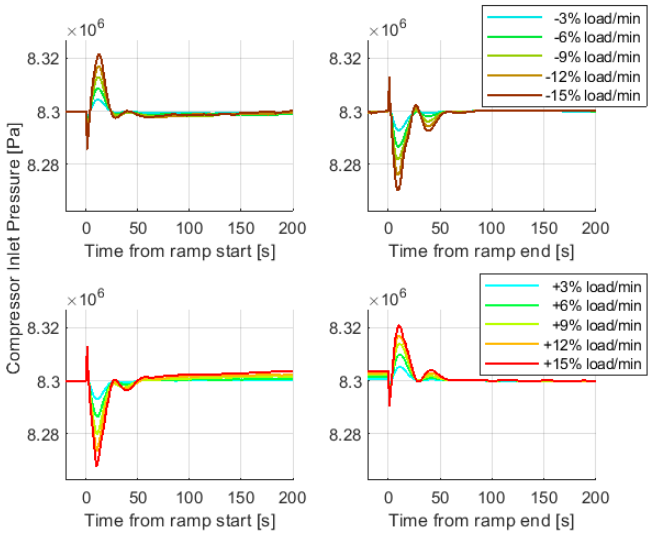

FIGURE 14: CIP BY RAMP PROGRESS AT VARIOUS RAMP RATES FOR A RAMP FROM 100% LOAD TO 50% LOAD (TOP, RAMP-DOWN) AND A RAMP FROM 50% LOAD TO 100% LOAD (BOTTOM, RAMP-UP)

Figure 15 shows the variation of the surge margin during a ramp-down in load (top) and a ramp-up in load (bottom) for various ramp rates, without any opening of the anti-surge valve. It can be observed that the offset from steady-state is proportional to the ramp rate, including its direction; during the fastest ramp-down in load, the maximum K_p offset is -0.057, while during the ramp-up of the same speed, the maximum K_p offset is +0.046. For the slowest ramp-down, the maximum offset was -0.007, which is near 8 times smaller for a ramp rate which was 10 times smaller.

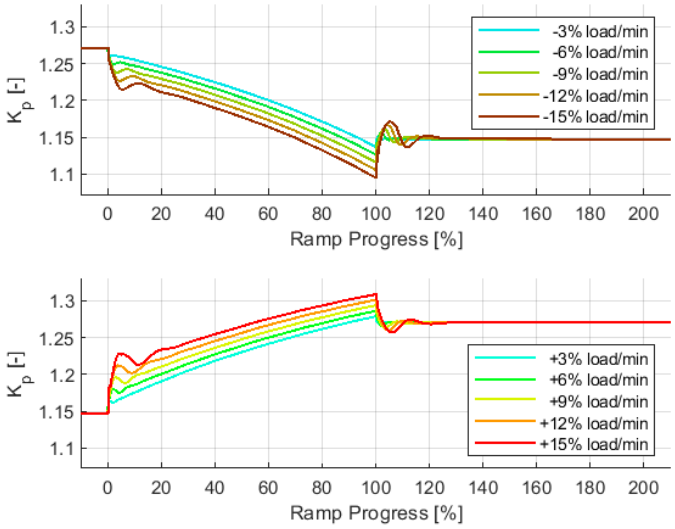

FIGURE 15: SURGE MARGIN BY RAMP PROGRESS FOR VARIOUS RAMP RATES.

During the ramp-downs, the turbine inlet pressure and mass flow steadily decrease in time, with little impact due to ramp rate. This decrease allows the turbine to be operated in the targeted off-design conditions by reduction of the pressure ratio and mass flow to limit its power output, while simultaneously maintaining its inlet temperature at design condition to retain high efficiency of the cycle. A value of about 143 bar at the turbine inlet is reached at 50% of the nominal load.

6. CONCLUSIONS

This study used a dynamic model to evaluate controller performance at various ramp rates for five key features of a simple recuperated supercritical-carbon-dioxide (sCO_2) Brayton cycle coupled with thermal energy from a concentrated solar power plant. Of the five main features, three can be well-controlled (within their manufacturer-recommended tolerance) with simple feedforward or feedback controls. The long (>300 s) settling time of the turbine inlet temperature (TIT) requires a combination of a feedforward and proportional-integral-derivative (PID) controller, while the nonlinear response of the compressor inlet pressure (CIP) requires a combination of a feedforward and feedback control, which is then added to a proportional-integral (PI) controller for best performance. The maximum mass flow through the inventory is also found to have a large impact on the maximum feasible ramp rate, since at faster ramp rates, the same amount of CO_2 should be added or removed in a shorter time frame. The inventory control for CIP is also found to be almost twice as effective at reducing pressure than it was at increasing pressure for any given mass flow rate of CO_2, requiring slightly greater mass flow rates from the inventory to increase the pressure than are required for venting to atmosphere. With a single control for the two valves, the disturbance in pressure due to compressor acceleration at the starts and ends of ramps is about 1.5 times as large in the negative direction (requiring addition of CO_2) than in the positive direction (requiring venting of CO_2). During ramp-downs, the surge margin decreases with augmenting ramp rate if all other controls are functional, while during ramp-ups, the surge margin increases by a similar proportion. This means that the ramp rate during a ramp-down in load is much more critical to surge risk than the ramp rate during a ramp-up in load, while sudden acceleration of the compressor may be more critical for regulation of the compressor inlet pressure.

The control system was demonstrated to be effective for multiple simulations of load variations. For a ramp from 100% to 50% of nominal load at a ramp rate of 15% per minute, the compressor inlet temperature was maintained within 0.02 K of its setpoint out of a margin of 1 K; the TIT was maintained within 0.17 K of its setpoint out of a margin of 5 K; and the compressor inlet pressure was maintained within +0.3 bar for increases in pressure, and within -0.4 bar for decreases in pressure, out of a tolerance of ±0.75 bar. For this ramp, the net power deviated by 2% of the nominal load, with an increase in deviation of about 0.13% of nominal load per 1%/min of ramp rate. It was also found that the steady-state surge margin, as well as the surge margin during ramps in load, could be reasonably predicted with the ramp rate and steady-state off-design maps in power.

As data from the demonstration plant becomes available, further comparison, validation, and finely-tuned control strategies can be developed to further minimize these errors and replicate the anti-surge valve control which is ultimately implemented in the plant.

ACKNOWLEDGEMENTS

This paper has been developed in the framework of the SOLARSCO2OL project. The SOLARSCO2OL project has received funding from the European Union's Horizon 2020 research and innovation program under grant agreement No 952953.

The authors would like to thank Chiara Barrili for the contribution to the development of the air cooler simulation model.

REFERENCES

[1] Manabe, S., 2019, "Role of Greenhouse Gas in Climate Change**," Tellus A Dyn. Meteorol. Oceanogr., **71**(1), p. 1620078.

[2] White, M. T., Bianchi, G., Chai, L., Tassou, S. A., and Sayma, A. I., 2021, "Review of Supercritical CO2

Technologies and Systems for Power Generation," Appl. Therm. Eng., **185**, p. 116447.

[3] Baik, Y. J., Kim, M., Chang, K. C., and Kim, S. J., 2011, "Power-Based Performance Comparison between Carbon Dioxide and R125 Transcritical Cycles for a Low-Grade Heat Source," Appl. Energy, **88**(3), pp. 892–898.

[4] Liu, Y., Wang, Y., and Huang, D., 2019, "Supercritical CO2 Brayton Cycle: A State-of-the-Art Review," Energy, **189**, p. 115900.

[5] Wright, S. A., Davidson, C. S., and Scammell, W. O., 2016, "Thermo-Economic Analysis of Four SCO2 Waste Heat Recovery Power Systems," *Fifth International SCO2 Symposium*, San Antonio, TX, pp. 28–31.

[6] Li, M. J., Jie, Y. J., Zhu, H. H., Qi, G. J., and Li, M. J., 2018, "The Thermodynamic and Cost-Benefit-Analysis of Miniaturized Lead-Cooled Fast Reactor with Supercritical CO2 Power Cycle in the Commercial Market," Prog. Nucl. Energy, **103**, pp. 135–150.

[7] Le Moullec, Y., 2013, "Conceptual Study of a High Efficiency Coal-Fired Power Plant with CO2 Capture Using a Supercritical CO2 Brayton Cycle," Energy, **49**(1), pp. 32–46.

[8] Yin, J. M., Zheng, Q. Y., Peng, Z. R., and Zhang, X. R., 2020, "Review of Supercritical CO2 Power Cycles Integrated with CSP," Int. J. Energy Res., **44**(3), pp. 1337–1369.

[9] Glos, S., Hansper, J., Grotkamp, S., and Wechsung, M., 2019, "Assessment of Performance and Costs of CO2 Based Next Level Geothermal Power (NLGP) Systems," 3rd Eur. Conf. Supercrit. CO2 Power Syst. 2019 19th-20th Sept. 2019, pp. 49–58.

[10] Alfani, D., Astolfi, M., Binotti, M., Silva, P., and Macchi, E., 2020, "Off-Design Performance of CSP Plant Based on Supercritical CO2 Cycles," AIP Conf. Proc., **2303**(1), p. 130001.

[11] Crespi, F., Sánchez, D., Rodríguez, J. M., and Gavagnin, G., 2020, "A Thermo-Economic Methodology to Select SCO2 Power Cycles for CSP Applications," Renew. Energy, **147**, pp. 2905–2912.

[12] Omar, A., Saldivia, D., Li, Q., Barraza, R., and Taylor, R. A., 2021, "Techno-Economic Optimization of Coupling a Cascaded MED System to a CSP-SCO2 Power Plant," Energy Convers. Manag., **247**, p. 114725.

[13] Van Der Westhuizen, R., and Dobson, R. T., 2019, "Modelling and Simulation of a Supercritical Carbon Dioxide (SCO2) Concentrated Solar Power (CSP) System," AIP Conf. Proc., **2126**(1), p. 140008.

[14] Lambruschini, F., Liese, E., Zitney, S. E., and Traverso, A., 2016, "Dynamic Model of a 10 MW Supercritical CO2 Recompression Brayton Cycle," *Proceedings of the ASME Turbo Expo - GT2016-56459*, American Society of Mechanical Engineers Digital Collection.

[15] Moisseytsev, A., and Sienicki, J. J., 2014, "Recent Developments in S-CO2 Cycle Dynamic Modeling and Analysis at ANL," *The 4th International Symposium-Supercritical CO 2 Power Cycles*, Pittsburgh, PA.

[16] "SOLARSCO2OL Project – SOLAR Based SCO2 Operating Low-Cost Plants" [Online]. Available: https://www.solarsco2ol.eu/. [Accessed: 14-Dec-2023].

[17] Gini, L., Maccarini, S., Traverso, A., Barberis, S., Guedez, R., Pesatori, E., and Bisio, V., 2023, "A Prototype Recuperated Supercritical Co2 Cycle: Part-Load and Dynamic Assessment," Appl. Therm. Eng., **225**, p. 120152.

[18] Gini, L., Maccarini, S., Traverso, A., Pesatori, E., Milani, A., Bisio, V., Valente, R., Barberis, S., and Guedez, R., 2022, "Part-Load Behaviour and Control Philosophy of a Recuperated Supercritical CO2 Cycle," *Proceedings of the ASME Turbo Expo - GT2022-83021*, American Society of Mechanical Engineers Digital Collection.

[19] Maccarini, S., Tucker, S., Mantelli, L., Barberis, S., and Traverso, A., 2023, "Dynamics and Control Implementation of a Supercritical CO2 Simple Recuperated Cycle," E3S Web Conf., **414**, p. 02012.

[20] Traverso, A., 2005, "TRANSEO Code for the Dynamic Performance Simulation of Micro Gas Turbine Cycles," *Proceedings of the ASME Turbo Expo - GT2005-68101*, pp. 45–54.

[21] Guedez, R., Guccione, S., Trevisan, S., Horta, P., Stengler, J., Martins, P., Meyer-Grünefeldt, M., Lopez-Roman, A., Barberis, S., and Xhani, I., 2022, "Demonstration of the SOLARSCO2OL SCO2 Power Cycle for Future Hybrid CSP-PV Plants at the Évora Molten Salt Platform," *28th International Conference on Concentrating Solar Power and Chemical Systems, SolarPACES*.

[22] Guédez, R., Barberis, S., MacCarini, S., López-Román, A., Milani, A., Pesatori, E., Oyarzábal, U., and Sánchez, A., 2022, "Design of a 2 MW Molten Salt Driven Supercritical CO2 Cycle and Turbomachinery for the SOLARSCO2OL Demonstration Project," *Proceedings of the ASME Turbo Expo - GT2022-82013*, American Society of Mechanical Engineers Digital Collection.

[23] Traverso, A., Massardo, A. F., and Scarpellini, R., 2006, "Externally Fired Micro-Gas Turbine: Modelling and Experimental Performance," Appl. Therm. Eng., **26**(16), pp. 1935–1941.

[24] White, C. W., Pidaparti, S., O'Connell, A. C., and Weiland, N., 2019, *Cooling Technology Models for Indirect SCO2 Cycles (No. NETL-PUB-22604)*, Pittsburgh, PA, Morgantown, WV, and Albany, OR (United States).

[25] Vojacekl, A., Melichar, T., Dostal, V., Goettelt, F., and Rohde, M., 2019, "Performance Test of the Air-Cooled Finned-Tube Supercritical CO2 Sink Heat Exchanger," J. Therm. Sci. Eng. Appl., **11**(3).

[26] Deshmukh, A., Kapat, J., and Khadse, A., 2021, "Transient Thermodynamic Modeling of Air Cooler in Supercritical CO2 Brayton Cycle for Solar Molten Salt

Application," J. Energy Resour. Technol. Trans. ASME, **143**(2).
[27] Wang, C. C., Chi, K. Y., and Chang, C. J., 2000, "Heat Transfer and Friction Characteristics of Plain Fin-and-Tube Heat Exchangers, Part II: Correlation," Int. J. Heat Mass Transf., **43**(15), pp. 2693–2700.
[28] Kays, W. M., and London, A. L., 1984, *Compact Heat Exchangers*.
[29] Cavallini, A., Del Col, D., Doretti, L., Matkovic, M., Rossetto, L., Zilio, C., and Censi, G., 2006, "Condensation in Horizontal Smooth Tubes: A New Heat Transfer Model for Heat Exchanger Design," Heat Transf. Eng., **27**(8), pp. 31–38.
[30] Gnielinski, V., 1975, "New Equations for Heat and Mass Transfer in the Turbulent Flow in Pipes and Channels," STIA, **41**(1), pp. 8–16.
[31] Casella, F., Mangola, G., and Alfani, D., 2020, "Density-Based Control of Air Coolers in Supercritical CO2 Power Cycles," IFAC-PapersOnLine, **53**(2), pp. 12554–12559.